Controlling the Al-Doping Profile and Accompanying Electrical Properties of Rutile-Phased TiO₂ Thin Films

Woojin Jeon,[†] Sang Ho Rha,[‡] Woongkyu Lee,[†] Yeon Woo Yoo,[†] Cheol Hyun An,[†] Kwang Hwan Jung,[§] Seong Keun Kim,[‖] and Cheol Seong Hwang*,[†]

[†]Department of Materials Science and Engineering and Inter-university Semiconductor Research Center, Seoul National University, Seoul 151-742, Republic of Korea

[‡] Process Development Team, Semiconductor R&D Center, Samsung Electronics Co. Ltd., Gyeonggi-do 446-712, Republic of Korea

[§]MEIS Dev. Team, Korea Materials & Analysis Corp., 554, Yongsan-Dong, Yusung-Gu, Daejeon 305-500, Republic of Korea

[‖]Electronic Materials Research Center, Korea Institute of Science and Technology, Seoul 136-791, Republic of Korea

ABSTRACT: The role of Al dopant in rutile-phased TiO₂ films in the evaluation of the mechanism of leakage current reduction in Al-doped TiO₂ (ATO) was studied in detail. The leakage current of the ATO film was strongly affected by the Al concentration at the interface between the ATO film and the RuO₂ electrode. The conduction band offset of the interface increased with the increase in the Al dopant concentration in the rutile TiO₂, which reduced the leakage current in the voltage region pertinent to the next-generation dynamic random access memory application. However, the Al doping in the anatase TiO₂ did not notably increase the conduction band offset even with a higher Al concentration. The detailed analyses of the leakage conduction mechanism based on the quantum mechanical transfer-matrix method showed that Schottky emission and Fowler–Nordheim tunneling was the dominant leakage conduction mechanism in the lower and higher voltage regions, respectively. The chemical analyses using X-ray photoelectron spectroscopy corroborated the electrical test results.

KEYWORDS: TiO₂, Al-doped TiO₂, leakage current, Schottky emission, conduction band offset, oxygen vacancy
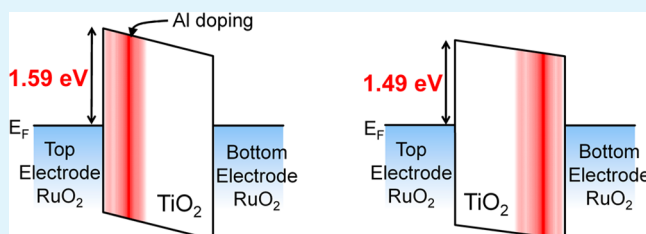
■ INTRODUCTION

Many high-dielectric-constant (κ) materials have been examined for capacitor application in the next-generation dynamic random access memory (DRAM).[1−3] The most important requirements for a capacitor dielectric have been a higher dielectric constant for higher capacitance and a lower leakage current density. At present, however, physical thinness ($\ll$10 nm) is also a critical requirement for use of the dielectric layer in the extremely narrow gap between the storage nodes in DRAMs with a design rule of <20 nm. It has been well-known that the dielectric constant and the leakage current have a trade-off relationship, and that higher-κ dielectric materials, such as rutile-structured TiO₂ and SrTiO₃, prevalently exhibit an exacerbated leakage current property due to their smaller band gap that results in generally lower band offsets with metal electrodes.[4] The ZrO₂/Al₂O₃/ZrO₂ (ZAZ) stack, which appears to offer a minimum equivalent oxide thickness (EOT) of ∼0.6 nm, is currently adopted for the capacitor dielectric of commercialized DRAM, with TiN as the top and bottom electrode.[5,6] However, as expected in the international technology roadmap for semiconductors, an even smaller EOT (down to 0.3 nm) with a leakage current density of <10⁻⁷ A/cm² at a capacitor voltage of 0.6 V will soon be required for the DRAM with a design rule of <20 nm. ZAZ is not expected to offer such a possibility due to its insufficient κ values. In

addition, TiN does not have a high enough work function (∼4.5 eV) for other higher κ dielectrics with a smaller band gap than the ZAZ material. The lower work function generally induces a smaller conduction band offset (CBO), which makes the leakage current higher. Furthermore, the oxidation of the TiN electrode especially at the interface with the high-κ dielectrics is expected to be aggravated when the high-κ dielectrics becomes a TiO₂-based material, because the binding energy between Ti and O is much weaker than between Zr and O, and Al and O. These factors indicate that another metal electrode is needed for next-generation DRAM capacitors.

To solve these technical issues, some of the authors reported the very promising electrical performance of Al-doped TiO₂ films (ATO)[7] grown on Ru and RuO₂ electrodes.[8,9] The ATO (also TiO₂) films were grown at relatively low process temperatures (200−300 °C). At these temperatures, the anatase phase, of which κ value and band gap are ∼40 and ∼3.4 eV, respectively, is thermodynamically stable. The anatase phase TiO₂ did not have any advantages over the ZrO₂. However, when the RuO₂ was adopted as the bottom electrode, the rutile phase TiO₂ material, the κ value, of which was proven

to be as high as ~100, was achieved via the local epitaxy-driven phase transition from anatase to rutile on the RuO_2.[10−12] RuO_2 has a rutile structure and a very favorable lattice match with rutile TiO_2. A minimum EOT of ~0.5 nm was achieved from such favorable aspects of the rutile ATO and rutile TiO_2.[7,11]

The general problem with rutile TiO_2 related to the leakage current, aside from its lower band gap of ~3.2 eV, is the easier formation of defects therein, mainly oxygen vacancy (V_o), due to the relatively weaker binding energy of the Ti−O bond. In fact, the band gap of 3.0−3.2 eV is not the main source of the leakage problem; the ~1.5−1.6 eV CBO and the valence band offset (VBO) when the E_F is located at the midgap position of the TiO_2 is sufficient to suppress the thermionic emission of the carriers from the electrode into the high-κ dielectric layer for a capacitor voltage of ~1 V. However, the presence of V_o's shifts the Fermi level (E_F) to the CB edge, which makes the CBO only ~1 eV,[7] and makes the capacitor vulnerable to the leakage current problem due to the thermionic emission. In addition, the defect level can mediate another carrier conduction mechanism, such as trap-assisted tunneling (TAT),[13] which further degrades the leakage performance. Doping the rutile TiO_2 with Al greatly mitigated such a problem by increasing the CBO, because Al ions generally work as acceptor centers in rutile TiO_2 and thereby balance the n- and p-type carriers.[7] This decreased the leakage current by 10^5-10^6 times at a capacitor voltage of ~0.8 V.[7]

The leakage current reduction by adopting Al_2O_3 in the high-κ dielectrics was reported to a certain degree in various high-κ dielectric materials, such as ZrO_2,[5,6,14] HfO_2,[15−17] and TiO_2.[18−23] However, rutile TiO_2 is the only material that has shown a significant decrease in its leakage current with a low atomic % of Al doping. Actually, the suggested leakage reduction mechanisms induced by Al differed depending on the high-κ materials. In the case of rutile TiO_2, as mentioned previously, the Al doping increased the CBO to its ideal value via the acceptor-like characteristic of the Al ions in the TiO_2. It was also unveiled that Al ions preferably present at the interface with the RuO_2 electrode even when the Al doping was performed in the middle of the ALD of the TiO_2 films.[7] In fact, this was a highly favorable aspect of the Al doping in the TiO_2 with the RuO_2 electrode, because the advantageous leakage reduction performance of the Al ions could be maximized when they are located at the interface, while the bulk of the rutile TiO_2 could maintain the higher-κ value due to the absence of Al ions in the bulk. This invoked an idea on the control of the Al distribution across the entire $RuO_2/TiO_2/RuO_2$ capacitor structure by varying the ALD cycle position of the Al_2O_3 among the ALD cycles of the TiO_2 film. Such variation can change the concentration of Al ions at both the top and bottom electrode interfaces, which may vary the thermionic emission effects. Therefore, in this research, an attempt was made to even more evidently evaluate the leakage current reduction mechanism in the rutile TiO_2 by changing the location of the Al doping throughout the dielectric film thickness while other parameters remained unchanged.

■ EXPERIMENT SECTION

The TiO_2 and ATO films were deposited using a traveling-wave-type ALD reactor at a wafer temperature of 250 °C. $Ti(OC_3H_7)_4$ (TTIP) and $Al(CH_3)_3$ (TMA) were used as the Ti and Al precursors, respectively, and O_3 with a concentration of 250 g/m^3 was used as the oxygen source. The TTIP pulse, purge, O_3 pulse, purge, TMA pulse, and purge times were 3, 5, 3, 5, 0.5, and 25 s, respectively. For the

growth of the rutile and anatase crystal structured TiO_2 films, RuO_2 (40 nm)/SiO_2 (100 nm)/Si and Pt (50 nm)/SiO_2 (100 nm)/Si substrates were adopted as the bottom electrode (BE) layers, respectively. The RuO_2 layer was deposited via chemical vapor deposition using $Ru(EtCp)_2$ and O_2 gases at a wafer temperature of 300 °C, and the Pt layer was DC-sputtered at a wafer temperature of 150 °C. To incorporate Al ions into the films, Al−O deposition cycles were introduced discretely into the film. The concentration of the Al along the thickness direction was changed by the location of only one Al−O deposition cycle among the 250 TiO_2 ALD cycles. To measure the electrical properties, the metal−insulator−metal (MIM) capacitor was fabricated with a 30 nm thick RuO_2 top electrode (TE) using a metal shadow mask (with a 300 μm hole diameter). On the RuO_2 TE, additional 50 nm thick Pt was deposited to improve the contact during the probing. The RuO_2 TE layer was deposited by DC reactive sputtering using an Ru metal target under an Ar/O_2 gas atmosphere. The TE deposition conditions were carefully optimized to minimize the sputter-damage effect on the high-κ dielectric layer, which was reported elsewhere.[24] After the TE deposition, postmetallization annealing (PMA) was performed at 400 °C for 30 min under a 95% N_2 + 5% O_2 atmosphere via a tube furnace. The film thickness was measured via spectroscopic ellipsometry (J. A. Woollam, ESM-300), X-ray fluorescence (XRF, Thermo Scientific, ARL Quant'X), and X-ray reflection (XRR, PANalytical, X'Pert Pro). The chemical composition of the film was characterized by time-of-flight secondary ion mass spectroscopy (ToF-SIMS, Cameca, IMS-4FE7) and time-of-flight medium energy ion scattering spectroscopy (ToF-MEIS, K-MAC, MEIS-K120) using a He-ion beam with an acceleration energy of 100 keV. The electronic state at the interface and the chemical composition were analyzed using X-ray photoemission spectroscopy (XPS, Sigma Probe). The electrical performance was studied by measuring the capacitance−voltage ($C-V$) and the current density− voltage ($J-V$) using the Hewlett-Packard 4140B and 4194A, respectively. The AC excitation frequency for the $C-V$ measurement was 10 kHz, and the capacitance values were taken at the DC bias voltage of 0 V. The estimated dielectric loss factor was generally <~2%, which confirms the accuracy of the capacitance estimation. For the evaluation of the electrical conduction mechanisms, the $J-V$ curves were measured at temperatures that ranged from 30 to 90 °C. During the electrical tests, the TE was biased and the BE was grounded.

■ RESULTS AND DISCUSSION

It was first confirmed that changing the location of one ALD Al_2O_3 cycle among the 250 ALD TiO_2 cycles can actually change the Al-doping profile within the 9 nm thick rutile TiO_2 films. For this purpose, three samples were prepared wherein the TiO_2 ALD cycles were divided into 20/230, 100/150, and 230/20 and the Al_2O_3 cycle intervened between the two consecutive groups of TiO_2 cycles. In other words, for the first sample, the 20 TiO_2 ALD cycles were deposited on the RuO_2 BE, one Al_2O_3 ALD cycle was deposited on the TiO_2 layer, and finally, 230 TiO_2 ALD cycles were deposited. These were called 20TA, 100TA, and 230TA, with the numbers indicating the TiO_2 cycle number before the single Al_2O_3 ALD cycle was commenced. The typical growth rates of TiO_2 and Al_2O_3 in this process are ~0.036 nm/cycle and ~0.1 nm/cycle, respectively. Therefore, approximately 0.72, 3.6, and 8.3 nm of TiO_2 films were deposited in each case, before the Al_2O_3 ALD cycle. It has been reported that the growth of the TiO_2 film on top of the Al_2O_3 layer was retarded compared with its growth on itself.[25] However, this retardation effect was limited to the ~5−10 cycles of TiO_2; as can be seen in the following section, the Al_2O_3 was indeed diffused into the underlying and over-depositing TiO_2 layers during the ALD, so that this retardation had a minimal effect on the overall film thickness. Therefore, the 250 TiO_2 ALD cycles and one Al_2O_3 ALD cycle resulted in
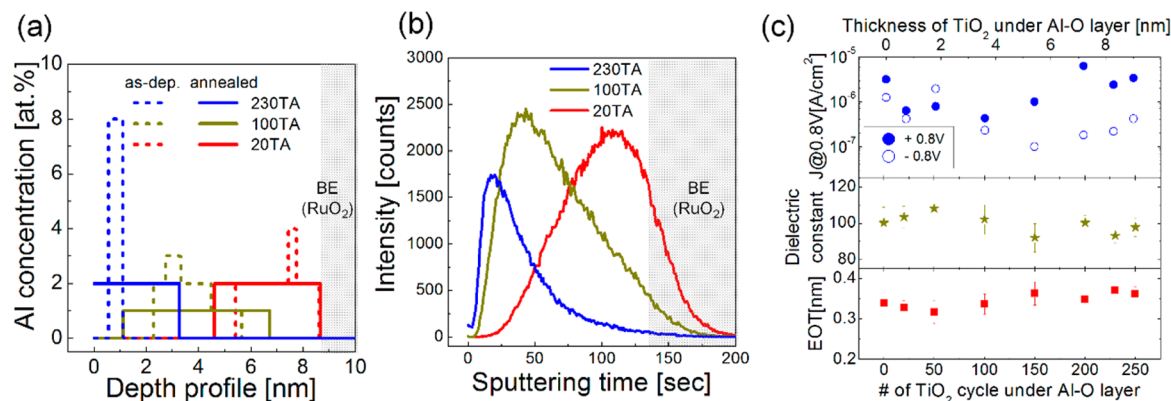
Figure 1. Al distributions across the ATO film of the as-deposited (dotted line) and after the postmetallization annealing (400 °C, 30 min, 95% N$_2$ + 5% O$_2$ in the tube furnace) condition (solid line), measured via (a) ToF-MEIS and (b) ToF-SIMS analyses, respectively. (c) Leakage current density change behavior as the distance between the bottom electrode and the Al insertion location when a positive sweep (injection of electrons from the bottom electrode, closed dot) and a negative sweep (injection of electrons from the top electrode, opened dot) were applied. The dielectric constant and EOT values of each sample are also depicted.

a ∼9 nm overall thickness, irrespective of the process sequences.

Figure 1a shows the ToF-MEIS profile of the Al before (dotted line) and after the annealing under the conditions identical to the PMA (solid line) of the three samples with no TE. Although the ToF-MEIS can quantitatively analyze the concentration of the Al doping even without appropriate standards, it has a limited atomic resolution, and the present samples generally have a low Al concentration, so that the depth profile in this analysis appears rather terse. However, the critical aspects of the Al profile can be identified well from these analyses, which makes them still important. The as-deposited samples showed Al concentration profiles that qualitatively agreed with the process sequences. 20TA had the highest Al concentration near the BE interface, which must be obviously understood from the proximity of the Al$_2$O$_3$ ALD cycle to the BE. Similarly, 100TA and 230TA showed the highest Al concentrations at the middle of the film and near the TE interface, respectively, thereby again corroborating the process sequence. However, it could also be noted that the Al concentration profile was significantly smeared, which reveals greater diffusion of Al ions into the bulk of the TiO$_2$ during the rather long ALD time (70 min) after the deposition of the Al–O layer on the 20-cycle TiO$_2$ in the case of 20TA, whereas 230TA showed a highly concentrated Al concentration profile at the TE interface, with negligible diffusion into the TiO$_2$ layer. This must be a natural consequence of the shorter period of time when the Al ions were exposed to the ALD temperature during the subsequent 20 TiO$_2$ cycles (6 min) in the case of 230TA. A notable finding from the Al concentration profiles is that they generally tend to be shifted onto the film surface. One possible reason could be that the solid solubility of Al in TiO$_2$ is quite limited (only a few wt % even under the high temperature and high pressure conditions,[26]) so that the temporarily quite high Al concentration immediately after the Al$_2$O$_3$ ALD cycle could be lowered by migrating Al ions on the surface of the overgrowing TiO$_2$ layer and lowering the system energy.[7] The less significant shift in the Al peak position toward the film surface of 20TA compared with that in 100TA may be ascribed to the tendency of Al to remain at the BE interface, where its energy is lower at the interface than in the bulk of the TiO$_2$.[7]

Such a tendency, i.e., of the Al ions to be preferably present closer to the surface (or the TE interface) than to the BE interface, was maintained after the annealing, although it certainly showed a more diffused concentration distribution (shown by the solid line in Figure 1a). The same could be confirmed from the ToF-SIMS profile in Figure 1b. It must be noted that the ToF-SIMS profile should not be taken quantitatively due to the lack of appropriate standards, so only the distribution profiles must be considered, and not even the relative comparison of the signal intensity. The ToF-MEIS and ToF-SIMS results confirmed that Al had the highest concentration near the TE and BE in 230TA and 20TA, respectively, after the PMA, and thus, must induce a higher CBO or Schottky barrier height (SBH) at those interfaces. 100TA had the highest Al concentration near the middle of the film, but is still believed to have a non-negligible Al doping concentration at both interfaces.

Figure 1c summarizes the electrical properties of the various samples after the PMA, where the ALD of Al$_2$O$_3$ was performed after the TiO$_2$ ALD cycles of 0, 20, 50, 100, 150, 200, 230, and 250, respectively. The results shown in Figure 1a,b make it obvious that the Al concentration must be higher at the TE (BE) interface, as the TiO$_2$ cycle number increased (decreased) before the ALD Al$_2$O$_3$ was commenced. The dielectric constant, which was estimated from the capacitance per area and the physical thickness of the films (9 nm), was almost independent of the Al$_2$O$_3$ ALD cycle position (100 ± 10). This value is already higher than the value reported for the ATO film with an average atomic concentration of ∼5–10%,[7] which could be ascribed to the generally much lower Al concentration in this study (∼1%, according to the ToF-MEIS). It must also be noted that the κ value in this estimation could have been influenced by the possible presence of the interfacial low-κ layer, so it could have been even higher when only the bulk portion of the κ was extracted from the inverse slope of the EOT vs the physical oxide thickness (POT) plot. This will be reported in the subsequent study. The figure also showed the EOT values for the various conditions, which were almost constant at 0.35 ± 0.02 nm. While the overall κ value did not notably change according to the Al$_2$O$_3$ cycle position, the J estimated at ±0.8 V (and at other voltages, as follows) certainly shows critical dependency on the Al$_2$O$_3$ cycle position. It must be noted that the MIM is basically a back-to-back diode structure, where the cathode interface plays a dominant role in controlling the electronic carrier injection as long as the
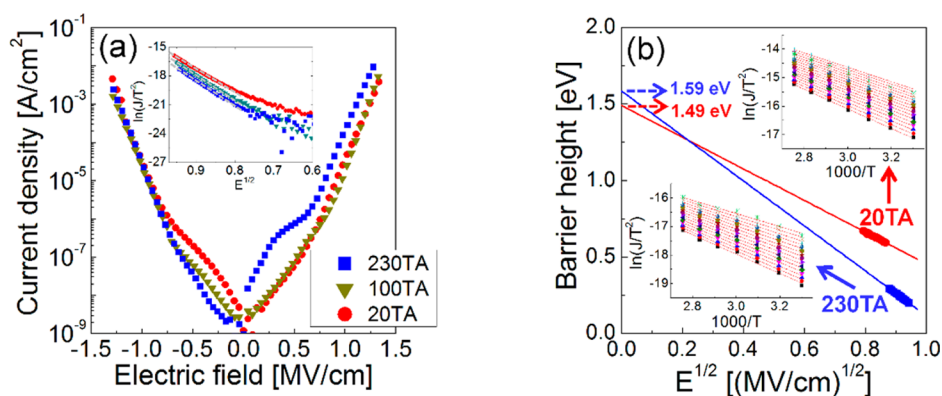
Figure 2. (a) $J-V$ curves of the ATO samples with various Al locations near the bottom electrode (20TA, red), at the middle of the film (100TA, yellow), and near the top electrode (230TA, blue); (inset) $\ln(J/T^2)$ vs $E^{1/2}$ plots of the low-electric-field region, where the negative bias was applied, to confirm the Schottky emission mechanism. (b) Fitting curves for the Schottky barrier height according to the modified Richardson−Schottky equation under the application of negative bias to the TE. The inset figures show the $\ln(J/T^2)$ vs $1000/T$ plots for 20TA (right upper panel) and 230TA (left bottom panel).

majority carriers are electrons, as in this study.[13,27,28] Therefore, for the positive (negative) TE bias, the BE (TE) interface governs the electron injection. Figure 1c clearly reveals that the J is lower when the cathode interface has a higher Al concentration, which is slightly more obvious for the TE interface. This coincides well with the previous reports that the Al ions at the electrode/rutile TiO_2 interface could increase the CBO, so that the SBH for the electron injection increases and the leakage current decreases.[7] The exceptions from these general trends were shown when the Al_2O_3 ALD was in direct contact with the RuO_2 BE or TE. These were supposed to have shown the lowest J for the positive and negative bias voltages because they had to induce the highest Al concentration at those interfaces, which was not necessarily the case. This revealed that a too high (local) Al concentration disrupts the (local) coherence between rutile RuO_2 and rutile TiO_2, and the higher density of interfacial defects eventually increases the leakage current. Therefore, a certain number of TiO_2 cycles (in this case, 20 cycles) must always intervene between the Al_2O_3 cycle and the RuO_2 TE and BE to achieve the optimum leakage current. A promising finding was that the samples with TiO_2 cycles of 100−150 before the Al_2O_3 cycle showed the lowest leakage current at both bias polarities. This could prove the presence of Al ions with appropriate concentrations at both interfaces via the diffusion of Al ions during the ALD and PMA steps. However, the even lower J level was achieved over a wider voltage range when the cathode interface had a higher Al concentration, as shown in Figure 2.

Figure 2a shows the $J-V$ curves of 20TA, 100TA, and 230TA in both bias polarities. They clearly show opposite trends in the positive and negative bias regions up to the absolute electric field ($|E|$) of ∼0.8 MV/cm, which was simply estimated by dividing the applied voltage by the film thickness. In the negative bias region, where the SBH at the TE interface mainly governed the J, 230TA showed the lowest J; but in the positive bias region, where the SBH at the BE interface mainly governed the J, 230TA showed the highest J. As 230TA must have had the highest Al concentration near the TE interface (Figure 1a,b), this could be understood from the higher and lower SBH values at the TE and BE interfaces. In contrast, 20TA showed exactly the opposite trend, which could also be well understood from the opposite distribution of the Al concentration. 100TA

showed intermediate $J-V$ behavior, as could be expected from the intermediate Al concentration distribution.

To quantitatively understand the electrical properties of the TE and BE interfaces, as well as the bulk properties of TiO_2, the $J-E$ curves were fitted to various current conduction models, such as Schottky emission, Poole−Frenkel (P−F) emission, Fowler−Nordheim (F−N) tunneling, and trap-assisted tunneling (TAT). Space charge limited conduction (SCLC) could be excluded because the interfaces generally block the carrier injection, whereas SCLC requires a heavily injecting interface.[29] The fitting procedure was generally very involved because it was unlikely that only a single conduction mechanism could cover the whole field region in this rather defect-involving the MIM system. Therefore, the various mechanisms were attempted first over the entire field region, and an appropriate field region was determined, considering not only the linearity of the data fit to the model, as exemplified in the inset of Figure 2a, where the fitting results according to the thermionic emission (the Schottky emission) are shown for the three samples, but also the extracted physical parameters, such as the optical dielectric constant in the Schottky fitting. After the significant effort to determine the most appropriate model for each sample in different E regions, the model that best fit the experiment results in the field region from 0 MV/cm to ∼0.8 MV/cm was found to be the Schottky emission, as shown in the inset of Figure 2a. The results of all the other single conduction models did not reasonably fit the experiment results, which means another method is needed to understand leakage conduction in a higher field. Such method will be shown later. For now, the $J-E$ in the low field region was taken as the representative example of the Al-doping effect on SBH.

To quantitatively estimate the zero-field SBH for the TE interfaces of 20TA and 230TA, which are supposed to show low and high values considering their low and high Al concentrations, respectively, at the TE interface, the $J-E$ curves were measured at various temperatures (T) that ranged from 303 to 363 K. The $\ln(J/T^2)$ values were plotted as functions of $1000/T$ for different E values that certainly belonged to the Schottky emission region, according to the following Schottky emission equations:

$$J = \frac{4\pi m^* q k^2 T^2}{h^3} \exp\left(-\frac{\phi_0}{kT}\right) \exp\left(\frac{\beta_S E^{1/2}}{kT}\right) \tag{1}$$

$$\ln\left(\frac{J}{T^2}\right) \propto -\frac{\phi_0}{kT} + \frac{\beta_S}{kT} E^{1/2} \tag{2}$$

where m^*, q, k, h, ϕ_0, β_s, ε_0, and κ_0 are the effective mass of the electron in the conduction band, the elementary charge, the Boltzmann constant, the Planck constant, the zero-field SBH, the Schottky constant given as $(q/4\pi\varepsilon_0\kappa_0)^{1/2}$, the vacuum permittivity, and the optical frequency dielectric constant, respectively. According to eq 2, the slope of each graph in the right upper panel and left bottom panel inset figures of Figure 2b, which correspond to 20TA and 230TA, respectively, coincide with $(\phi_0 - \beta_s E^{1/2})/k$ at each $E^{1/2}$, and the plot of $(\phi_0 - \beta_s E^{1/2})/k$ vs $E^{1/2}$, as shown in Figure 2b, gives the ϕ_0 (y-axis intercept) and κ_0 (slope). The achieved ϕ_0 values for 20TA and 230TA were 1.49 and 1.59 eV, respectively, and κ_0 was commonly 5.3. The achieved κ_0 of 5.3 was close to the optically estimated value of the refractive index ($\kappa_0 = n^2$, where n is the refractive index), which could be estimated using spectroscopic ellipsometry [$n = 2.6$–2.7] which suggests the validity of Schottky fitting in the E and T regions. In addition, the highly linear trends of the graphs in the inset figures of Figure 2b corroborate the validity of the Schottky model. Therefore, it could be understood that the Al doping at the interface with the RuO$_2$ electrode efficiently increased the SBH (by ∼0.1 eV) and suppressed the leakage current. The 0.1 eV increment is much smaller than what has been reported for the comparison of the undoped TiO$_2$ (ϕ_0, ∼1.0 eV) with the 5–10% Al-doped ATO (∼1.5 eV).[7,12] This suggests that the TE interface of 20TA also has a non-negligible Al concentration, which in fact already increased the SBH to ∼1.5 eV. However, the further increase in the Al concentration at the TE interface in the case of 230TA further increased the SBH by ∼0.1 eV, which in turn further decreased the leakage current. It must be noted that ∼1.6 eV is the highest attainable SBH because the band gap of rutile TiO$_2$ is ∼3.2 eV.

It can be argued that the SBH at the BE interface could be estimated from the similar analysis of the J–E curves in the positive bias region, and a lower SBH must be achieved than that at the TE interface in the case of 230TA, because the Al concentration of this sample must be higher and lower at the TE and BE interfaces, respectively. However, the J–E analysis in the positive bias region was not straightforward due to the involvement of the internal bias field that originated from the different SBH's at both interfaces. Because the SBH at the TE is supposed to be higher than that at the BE, there must be a certain (positive) voltage to compensate for the internal bias, which could be regarded as a barrier height difference between the two interfaces ($\Delta\phi$), and the current conduction cannot follow the Schottky emission up to the $\Delta\phi$. The presence of such $\Delta\phi$ distorts the J–E curves, and a relatively slow increase in J with an increasing E (hump) could be seen in the positive bias region in Figure 2a in the case of 230TA. As shown in the following figure, the voltage region where the aforementioned hump is shown was determined by the amount of the $\Delta\phi$, so it could be a reasonable way to estimate the difference in the SBH values at the two interfaces. The best fit of the asymmetric J–E curves was achieved (see Figure 3) when the $\Delta\phi$ was assumed to be ∼0.3 eV in 230TA. This suggests that the SBH at the BE interface was ∼1.3 eV, which is lower than that at the TE of
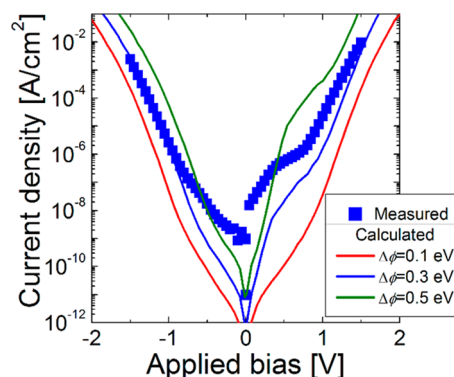

Figure 3. J–E curves of the 230TA films measured at 300 K (blue square points). The lines show the quantum mechanical fitting results using the parameters mentioned in the text. The difference among these lines is the barrier height difference ($\Delta\phi$); and the red, blue, and green lines represent the $\Delta\phi$ values of 0.1, 0.3, and 0.5 eV, respectively.

20TA (∼1.5 eV). When the deposition sequence and the common RuO$_2$ is considered as both the TE and BE, the ideal SBH's at the TE interface of 20TA and the BE of 230TA are supposed to be identical. However, the actual interfacial SBH could be influenced by many other factors that could influence the position of E_F as well as the work function of RuO$_2$, so that this may not be the case. Furthermore, as can be clearly understood from the concentration profiles of 230TA and 20TA in Figure 1a,b, the Al concentration at the BE interface of 230TA must be lower than that at the TE interface of 20TA. Therefore, the lower SBH at the BE interface of 230TA compared with that at the TE interface of 20TA appears very reasonable. Similarly, the difference in the SBH values at the TE and BE interfaces must be lower in 20TA than in 230TA, because the Al concentration at the TE interface must be higher than that at the BE interface in 230TA. This could be indirectly confirmed from the much less obvious J–V asymmetry of 20TA shown in Figure 2a. The J–E curve of 100TA showed a much more symmetric shape, which could be expected from the more symmetric, albeit still slightly asymmetric, Al concentration distribution in the film.

The J–V behavior of 230TA was further examined via quantum mechanical simulation based on the transfer-matrix method, which Jonsson et al. and Tsu et al. recently suggested.[30,31] The details of such J–V simulations have been reported elsewhere for the undoped rutile TiO$_2$ and TiO$_2$/thin HfO$_2$ bilayer cases.[13] In short, the basic principle behind the transfer-matrix method is the approximation of an arbitrarily shaped energy barrier as a series of thin piecewise constant barriers. Because the electron wave function in each of the piecewise constant barriers can be readily calculated, the total transfer matrix is derived through a number of subsequent matrix computations. Then the transmission coefficient of the overall energy barrier can be derived from this transfer matrix.[30,31] The primary advantage of this method is that it can be easily extended to other material systems, such as the RuO$_2$/Al-doped TiO$_2$/RuO$_2$ in this study, by changing the pertinent physical parameters. In this quantum mechanical simulation, the Schottky emission mechanism, TAT, and the F–N tunneling mechanism were considered with the parameters that affect the J level, namely, the ϕ_0, band conduction and tunneling effective mass of electrons (m^*, $m_{e,t}^*$), trap density (n_t) and their energy level in the band gap
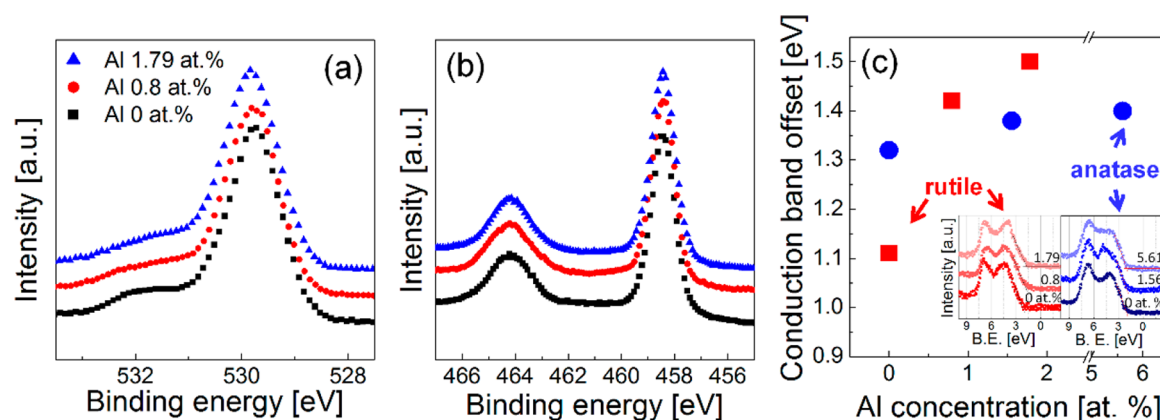
Figure 4. XPS spectra of the rutile-phased TiO_2 film surface with various Al concentrations of (a) O 1s and (b) a Ti 2p core levels, respectively. (c) Variation of the conduction band offset as a function of the Al concentration of rutile (red) and anatase (blue) TiO_2. The left and right panels of the inset show the valence band spectra of the rutile and anatase TiO_2 films, respectively.

(ϕ_t), and the dielectric constant at the optical frequency (κ_0) and a low frequency (κ_l). Here, κ_0 affects the system through the image force effect. κ_l has no effect on single-layered dielectrics but influences the voltage distribution between the two dielectric layers in a bilayer sample or the dielectric layers with nonhomogeneous κ values along the film thickness direction. Although in this experiment, a single dielectric layer (Al-doped TiO_2) was adopted, realistic MIM capacitors always have a multiple-layered dielectric structure due to the interfacial dead-layer effect, and a nonuniform Al concentration across the thickness. However, these factors were not significantly considered in this simulation, which might have caused a certain discrepancy between the experimental and simulated $J-V$ curves especially in the low-voltage region. It was found that Schottky emission and F−N tunneling mostly account for the current conduction in low- and high-voltage regions, respectively. Therefore, TAT was not considered in this study.

Figure 3 compares the experimental $J-V$ curve of 230TA, measured at 300 K (filled triangular symbols), with the simulated $J-V$ curves, assuming the $\Delta\phi$ of 0.1, 0.3, and 0.5 V. The other parameters for the simulations are as follows: $\phi_0 = 0.95$ eV, $m^* = 5\ m_o$, $m_{e,t}^* = 0.15\ m_o$, $\kappa_0 = 5.3$, and $\kappa_l = 100$. The detailed analysis of the fitting results showed that the J at the higher absolute voltages ($< \sim -1$ V or $> \sim +1$ V) was mainly governed by the F−N tunneling mechanism. On the other hand, the J in the lower absolute voltages was dominated by the Schottky emission mechanism. However, the absolute values of the simulated J could not be well matched with the experimental J in the low-voltage region, mainly due to the aforementioned reason. Although the theory assumed a uniform κ_l value so that in a uniform electric field, given as the V/film thickness, the actual electric field at the cathode interface must be slightly higher than that due to the presence of an interfacial low dielectric layer (a slightly higher field at the interface while the field in bulk must be slightly lower). Moreover, a nonhomogeneous Al distribution might also affect the electric field distribution. A similar problem was observed in the other case.[13] Nevertheless, the overall $J-V$ trend could be reproduced well by the simulation, including the asymmetry in the bias polarity dependency and the presence of a hump near ~ 0.5 V when the $\Delta\phi$ of 0.3 V was taken. This confirmed that the SBH values at the TE and BE estimated from the fitting to

the Schottky model were correct, and the understanding of the Al-doping effect on the SBH was reasonable.

Finally, the possible variations in the chemical states of the TiO_2 films due to the Al doping were examined using XPS core-level and VB analyses. For such analyses, another set of TiO_2 and ATO films with a total thickness of ~ 10 nm were deposited with the Al concentrations of 0%, 0.8%, and 1.8% ([Al]/([Al] + [Ti])), which were estimated from the XPS spectra. For uniform Al doping, the ALD Al_2O_3 and TiO_2 cycles were deposited in the following sequence: 50 TiO_2 cycles + 1 Al_2O_3 cycle + 100 TiO_2 cycles + 1 Al_2O_3 cycle + 100 TiO_2 cycles + 1 Al_2O_3 cycle + 50 TiO_2 cycles (for a total of 300 TiO_2 cycles and 3 Al_2O_3 cycles) for the sample with a lower Al concentration, and (50 TiO_2 cycles + 1 Al_2O_3 cycle) × 5 times + 50 TiO_2 cycles (for a total of 300 TiO_2 cycles and 5 Al_2O_3 cycles) for the sample with a higher Al concentration. Figure 4a shows the O 1s core-level spectra of the Al-doped films. It can be understood that the peak came to have a slightly broader shape mainly due to the addition of the O 1s component at the higher binding energy, which could have been assigned to the oxygen ions combined with Al. In contrast, the Ti 2p spectra of the three samples, as shown in Figure 4b, revealed no difference within the experimental error of the XPS tool. Therefore, it could be concluded that the Al dopant in TiO_2 did not induce a significant chemical change within the examined doping concentration level.

This certainly contradicts the $J-V$ results shown in Figures 1 and 2, because the V_o was generally considered the source trap, which degraded the leakage current. Therefore, precise understanding of the role of Al doping in TiO_2 for decreasing the leakage current is needed. When an Al_2O_3 molecule is substituted for two TiO_2 units, one oxygen vacancy and two Al_{Ti} are formed, according to the Kröger-Vink notation, wherein Al_{Ti} represents the Ti site occupied by Al ions. In rutile TiO_2, the energy difference between the V_o and the CB edge is usually small (~ 0.5 eV),[32] which makes it vulnerable to exciting the electrons from the neutral V_o to CB (i.e., V_o ionize to V_o^{+2} via the V_o^+ state).[33] The energy position of V_o^{+2} is within the CB, so it no longer affects the electrical properties. This was accompanied by the increase in the electron concentration in the CB, which shifted the E_F from its neutral position to the CB edge. However, when there were Al_{Ti}, the energy level of which was only ~ 0.46 eV from the VB edge,[34] these Al_{Ti} accepted electrons from the V_o, which could have

shifted the E_F toward the VB edge direction. Therefore, even though Al doping in TiO_2 produced V_o's, the excess electrons associated with them could be localized at the Al_{Ti} sites (two electrons from one V_o, as one electron can be trapped at each Al_{Ti} site). Although the Al doping could not decrease the V_o concentration due to the nonstoichiometry of the TiO_2 itself (in fact, the neutral V_o density increases according to the Al doping, as just mentioned), the E_F could be shifted toward the center of the band gap, which would increase the SBH. This could appropriately explain the increase in the SBH (or the ϕ_0) via the Al doping in the experiment. This was further confirmed by the VB spectra in the XPS and the extracted CBO when the band gap of 3.2 eV in the rutile TiO_2 was assumed. The VB spectra of the undoped and the 0.8% and 1.8% Al-doped TiO_2 films are shown in the left panel of the inset of Figure 4c. From the extrapolation of the VB spectra to the background intensity line, the VBO was estimated. The variations in the CBO as a function of the Al concentration are summarized in Figure 4c. Here, the zero point of the binding energy was taken as the ground potential of the XPS system, which was equilibrated with the E_F of bottom RuO_2 layer. Therefore, these VB spectra could accurately show the VBO. It could be clearly seen that the increased Al concentration increased the CBO, and that the increase in the CBO between the 0.8% and 1.8% Al-doped TiO_2 films was ~0.1 eV, which is very similar to the extracted SBH from the Schottky fitting, as shown in Figure 2. The VB estimation of thinner thickness (2 nm) films showed similar results (data not shown).

The role of Al doping in TiO_2 could be seen from the similar doping and XPS VB experiments on the anatase–TiO_2 film grown on the Pt electrode. When the TiO_2 (and ATO) films were grown on the Pt electrode via the identical ALD processes, the crystallographic phase of the films was anatase, which was thermodynamically stable under the growth condition, because there could be no local epitaxy-driven phase transition.[11] The right panel of the inset of Figure 4c shows the VB spectra in the XPS of the 0%, 1.6%, and 5.6% Al-doped anatase–TiO_2 films. The VBO was estimated in a similar manner; and from the assumption of a band gap of 3.4 eV in the anatase–TiO_2,[35,36] the CBO was estimated as shown in Figure 4c. In contrast to the rutile TiO_2 case, it can be understood that the CBO did not show a notable variation even with a larger increase in the Al concentration (1.3–1.4 eV). To understand this inconsistent behavior of the anatase–TiO_2 compared with rutile–TiO_2, the energy band structure of the anatase–TiO_2 with V_o and Al_{Ti} was examined from literature. It was reported that a neutral V_o formed an energy level within the band gap of ~0.7 eV apart from the CB edge,[36] and Al_{Ti} formed an energy level of ~0.53 eV below the V_o level in anatase–TiO_2.[34] The ~0.7 eV is too high for the trapped electrons at V_o to be excited to the CB, which made the materials less n-type (the E_F remained near the midgap position). Even when the Al_{Ti} centers formed and accepted electrons from the V_o levels, their influence on the E_F position must be minimal because the energy level of Al_{Ti} is still higher than the midgap energy level. Only a slight decrease in the E_F could be expected, which corresponded well with the small SBH increase (or CBO increase) in this case.

CONCLUSION

In conclusion, the Al-doping profiles in Al-doped rutile TiO_2 were controlled by varying the ALD sequence of the dielectric film growth, where the films were grown on a RuO_2 electrode at a substrate temperature of 250 °C. While the Al ions were diffused to a certain degree into the TiO_2 layer, the main location of the Al dopant was adjusted near the top, bottom, and middle positions of the films. The Al ions tended to move toward the top electrode, which might be ascribed to the higher affinity of the Al ions to oxygen (or O_3) atoms during the ALD growth of the subsequent TiO_2 layers. When the Al doping was conducted near the top electrode interface, the Schottky barrier height increased to ~1.6 eV, which is the optimum value needed to suppress both the electron and hole injections. In contrast, the opposite interface appeared to have a Schottky barrier height of only ~1.3 eV, which induced severe asymmetry in the $J–V$ curve of the MIM capacitor with the RuO_2 top and bottom electrodes. Due to the minimum Al concentration level (1 Al_2O_3 ALD cycle among the 250 TiO_2 ALD cycles to grow a 9 nm thick dielectric film), the overall dielectric constant was kept at ~100 ± 10, irrespective of the doping location. The XPS VB analyses showed good consistency with the CBO values estimated from the chemical and electrical analyses. The energy levels of the V_o and Al_{Ti} in the band gap could explain very well the CBO results not only in the rutile TiO_2 but also in the anatase TiO_2. It could be understood that increasing the interfacial Al concentration by locating the Al_2O_3 ALD cycle position near the top and bottom interfaces while keeping the Al concentration as low as possible in the bulk film is an efficient method of suppressing the leakage current without sacrificing the dielectric constant of rutile TiO_2 films.

AUTHOR INFORMATION

Corresponding Author

*C. S. Hwang. E-mail: cheolsh@snu.ac.kr. Tel: 82-2-882-7535.

Notes

The authors declare no competing financial interest.

REFERENCES

(1) Kim, S. K.; Lee, S. W.; Han, J. H.; Lee, B.; Han, S.; Hwang, C. S. Capacitors with an Equivalent Oxide Thickness of < 0.5 nm for Nanoscale Electronic Semiconductor Memory. *Adv. Funct. Mater.* **2010**, *20* (18), 2989−3003.

(2) Hwang, C. S. *Atomic Layer Deposition of Nanostructured Materials: Atomic Layer Deposition for Microelectronic Applications*; Wiley-VCH Verlag GmbH & Co. KGaA: Weinheim, Germany, 2011; pp 159−192.

(3) Hwang, C. S. *Atomic Layer Deposition for Semiconductors*; Springer US: New York, 2014.

(4) Robertson, J. Band Offsets of Wide-band-gap Oxides and Implications for Future Electronic Devices. *J. Vac. Sci. Technol. B* **2000**, *18* (3), 1785−1791.

(5) Cho, H. J.; Kim, Y. D.; Park, D. S.; Lee, E.; Park, C. H.; Jang, J. S.; Lee, K. B.; Kim, H. W.; Chae, S. J.; Ki, Y. J.; Han, I. K.; Song, Y. W. New TIT Capacitor with $ZrO_2/Al_2O_3/ZrO_2$ Dielectrics for 60nm and below DRAMs, *Proceeding of the 36th European Solid-State Device Research Conference (ESSDERC)*, Montreux, Switzerland, Sept. 19−21,

2006; Institute of Electrical and Electronics Engineers: New York, 2006.

(6) Kil, D.-S.; Song, H.-S.; Lee, K.-J.; Hong, K.; Kim, J.-H.; Park, K.-S.; Yeom, S.-J.; Roh, J.-S.; Kwak, N.-J.; Sohn, H.-C.; Kim, J.-W.; Park, S.-W. Development of New TiN/ZrO₂/Al₂O₃/ZrO₂/TiN Capacitors Extendable to 45nm Generation DRAMs Replacing HfO₂ Based Dielectrics, *Symposium on VLSI Technology*, Honolulu, USA, June 13–15, 2006.

(7) Kim, S. K.; Choi, G. J.; Lee, S. Y.; Seo, M.; Lee, S. W.; Han, J. H.; Ahn, H. S.; Han, S.; Hwang, C. S. Al-doped TiO₂ Films with Ultralow Leakage Currents for Next Generation DRAM Capacitors. *Adv. Mater.* **2008**, *20* (8), 1429–1435.

(8) Han, J. H.; Lee, S. W.; Choi, G.-J.; Lee, S. Y.; Hwang, C. S.; Dussarrat, C.; Gatineau, J. Chemical Vapor Deposition of Ru Thin Films with an Enhanced Morphology, Thermal Stability, and Electrical Properties Using a RuO₄ Precursor. *Chem. Mater.* **2008**, *21* (2), 207–209.

(9) Han, J. H.; Lee, S. W.; Kim, S. K.; Han, S.; Hwang, C. S.; Dussarrat, C.; Gatineau, J. Growth of RuO₂ Thin Films by Pulsed-Chemical Vapor Deposition Using RuO₄ Precursor and 5% H₂ Reduction Gas. *Chem. Mater.* **2010**, *22* (20), 5700–5706.

(10) Choi, G.-J.; Kim, S. K.; Won, S.-J.; Kim, H. J.; Hwang, C. S. Plasma-Enhanced Atomic Layer Deposition of TiO₂ and Al-Doped TiO₂ Films Using N₂O and O₂ Reactants. *J. Electrochem. Soc.* **2009**, *156* (9), G138–G143.

(11) Kim, S. K.; Kim, W. D.; Kim, K. M.; Hwang, C. S.; Jeong, J. High Dielectric Constant TiO₂ Thin Films on a Ru Electrode Grown at 250 Degrees C by Atomic-Layer Deposition. *Appl. Phys. Lett.* **2004**, *85* (18), 4112–4114.

(12) Han, J. H.; Han, S.; Lee, W.; Lee, S. W.; Kim, S. K.; Gatineau, J.; Dussarrat, C.; Hwang, C. S. Improvement in the Leakage Current Characteristic of Metal-Insulator-Metal Capacitor by Adopting RuO₂ Film as Bottom Electrode. *Appl. Phys. Lett.* **2011**, *99*, 022901.

(13) Seo, M.; Rha, S. H.; Kim, S. K.; Han, J. H.; Lee, W.; Han, S.; Hwang, C. S. The Mechanism for the Suppression of Leakage Current in High Dielectric TiO₂ Thin Films by Adopting Ultra-Thin HfO₂ Films for Memory Application. *J. Appl. Phys.* **2011**, *110*, 024105.

(14) Zhou, D.; Schroeder, U.; Xu, J.; Heitmann, J.; Jegert, G.; Weinreich, W.; Kerber, M.; Knebel, S.; Erben, E.; Mikolajick, T. Reliability of Al₂O₃-doped ZrO₂ High-k Dielectrics in Three-Dimensional Stacked Metal-Insulator-Metal Capacitors. *J. Appl. Phys.* **2010**, *108*, 124104.

(15) Ding, S.-J.; Zhu, C.; Li, M.-F.; Zhang, D. W. Atomic-Layer-Deposited Al₂O₃–HfO₂–Al₂O₃ Dielectrics for Metal-Insulator-Metal Capacitor Applications. *Appl. Phys. Lett.* **2005**, *87*, 053501.

(16) Kukli, K.; Ritala, M.; Leskelä, M.; Sajavaara, T.; Keinonen, J.; Gilmer, D.; Hegde, R.; Rai, R.; Prabhu, L. Atomic Layer Deposition of HfO₂ Thin Films and Nanolayered HfO₂–Al₂O₃–Nb₂O₅ Dielectrics. *J. Mater. Sci.: Mater. Electron.* **2003**, *14* (5–7), 361–367.

(17) Suzuki, R.; Taoka, N.; Yokoyama, M.; Lee, S.; Kim, S. H.; Hoshii, T.; Yasuda, T.; Jevasuwan, W.; Maeda, T.; Ichikawa, O.; Fukuhara, N.; Hata, M.; Takenaka, M.; Takagi, S. 1-nm-Capacitance-Equivalent-Thickness HfO₂/Al₂O₃/InGaAs Metal-Oxide-Semiconductor Structure with Low Interface Trap Density and Low Gate Leakage Current Density. *Appl. Phys. Lett.* **2012**, *100*, 132906.

(18) Ahn, J.; Geppert, I.; Gunji, M.; Holland, M.; Thayne, I.; Eizenberg, M.; McIntyre, P. C.; Titania/Alumina Bilayer, Gate Insulators for InGaAs Metal-Oxide-Semiconductor Devices. *Appl. Phys. Lett.* **2011**, *99*, 232902.

(19) Jeon, W.; Chung, H.-S.; Joo, D.; Kang, S.-W. TiO₂/Al₂O₃/TiO₂ Nanolaminated Thin Films for DRAM Capacitor Deposited by Plasma-Enhanced Atomic Layer Deposition. *Electrochem. Solid-State Lett.* **2008**, *11* (2), H19–H21.

(20) Jõgi, I.; Kukli, K.; Kemell, M.; Ritala, M.; Leskelä, M. Electrical Characterization of AlₓTiᵧOₓ Mixtures and Al₂O₃–TiO₂–Al₂O₃ Nanolaminates. *J. Appl. Phys.* **2007**, *102*, 114114.

(21) Kim, Y. S.; Jin Yun, S. Nanolaminated Al₂O₃–TiO₂ thin films grown by atomic layer deposition. *J. Cryst. Growth* **2005**, *274* (3–4), 585–593.

(22) Lee, W.; Han, J. H.; Lee, S. W.; Han, S.; Jeon, W. J.; Hwang, C. S. Controlling the Initial Growth Behavior of SrTiO₃ Films by Interposing Al₂O₃ Layers Between the Film and the Ru Substrate. *J. Mater. Chem.* **2012**, *22* (30), 15037–15044.

(23) Rowlette, P. C.; Wolden, C. A. Pulsed Plasma-Enhanced Chemical Vapor Deposition of Al₂O₃–TiO₂ Nanolaminates. *Thin Solid Films* **2010**, *518* (12), 3337–3341.

(24) Kim, H. K.; Yu, I. H.; Lee, J. H.; Park, T. J.; Hwang, C. S. Controlling Work Function and Damaging Effects of Sputtered RuO₂ Gate Electrodes by Changing Oxygen Gas Ratio during Sputtering. *ACS Appl. Mater. Interfaces* **2013**, *5* (4), 1327–1332.

(25) Kim, S. K.; Choi, G. J.; Kim, J. H.; Hwang, C. S. Growth Behavior of Al-doped TiO₂ Thin Films by Atomic Layer Deposition. *Chem. Mater.* **2008**, *20* (11), 3723–3727.

(26) Escudero, A.; Langenhorst, F.; Müller, W. F. Aluminum Solubility in TiO₂ Rutile at High Pressure and Experimental Evidence for a CaCl₂-Structured Polymorph. *Am. Mineral.* **2012**, *97* (7), 1075–1082.

(27) Shin, J. C.; Park, J.; Hwang, C. S.; Kim, H. J. Dielectric and Electrical Properties of Sputter Grown (Ba,Sr)TiO₃ Thin Films. *J. Appl. Phys.* **1999**, *86* (1), 506–513.

(28) Hwang, C. S.; Joo, S. H. Variations of the Leakage Current Density and the Dielectric Constant of Pt/(Ba,Sr)TiO₃/Pt Capacitors by Annealing Under a N₂ Atmosphere. *J. Appl. Phys.* **1999**, *85* (4), 2431–2436.

(29) Rose, A. Space-Charge-Limited Currents in Solids. *Phys. Rev.* **1955**, *97* (6), 1538–1544.

(30) Jonsson, B.; Eng, S. Solving the Schrodinger Equation in Arbitrary Quantum-Well Potential Profiles Using the Transfer Matrix Method. *IEEE J. Quantum Electron.* **1990**, *26* (11), 2025–2035.

(31) Tsu, R.; Esaki, L. Tunneling in a Finite Superlattice. *Appl. Phys. Lett.* **1973**, *22* (11), 562–564.

(32) He, J.; Behera, R. K.; Finnis, M. W.; Li, X.; Dickey, E. C.; Phillpot, S. R.; Sinnott, S. B. Prediction of High-Temperature Point Defect Formation in TiO₂ From Combined ab initio and Thermodynamic Calculations. *Acta Mater.* **2007**, *55* (13), 4325–4337.

(33) Janotti, A.; Varley, J. B.; Rinke, P.; Umezawa, N.; Kresse, G.; Van de Walle, C. G. Hybrid Functional Studies of the Oxygen Vacancy in TiO₂. *Phys. Rev. B* **2010**, *81* (8), 085212.

(34) Deák, P.; Aradi, B.; Frauenheim, T. Polaronic Effects in TiO₂ Calculated by the HSE06 Hybrid Functional: Dopant Passivation by Carrier Self-Trapping. *Phys. Rev. B* **2011**, *83* (15), 155207.

(35) Tang, H.; Lévy, F.; Berger, H.; Schmid, P. E. Urbach Tail of Anatase TiO₂. *Phys. Rev. B* **1995**, *52*, 7771–7774.

(36) Di Valentin, C.; Pacchioni, G.; Selloni, A. Reduced and n-Type Doped TiO₂: Nature of Ti³⁺ Species. *J. Phys. Chem. C* **2009**, *113* (48), 20543–20552.